JOURNAL OF GEOPHYSICAL RESEARCH, VOL. 117, C12017, doi:10.1029/2012JC008257, 2012

Atmospheric infrasound from nonlinear wave interactions during Hurricanes Felicia and Neki of 2009

Justin E. Stopa,[1] Kwok Fai Cheung,[1] Milton A. Garcés,[2] and Nickles Badger[2]

Received 5 June 2012; revised 5 September 2012; accepted 19 October 2012; published 13 December 2012.

[1] Monitoring stations around the globe routinely detect microbarom signals with a dominant frequency of ∼0.2 Hz from regions of marine storminess. International Monitoring System (IMS) infrasound array IS59 in Kailua-Kona, Hawaii recorded clear signals in close proximity of Hurricanes Felicia and Neki of 2009 for a first-hand investigation of the detailed source mechanism through a hindcast analysis. A spectral wave model describes the tropical cyclone and ambient sea states through a system of two-way nested grids with forcing from a blended data set of global, regional, and cyclonic winds. The computed wave conditions are validated with altimetry measurements and utilized in an acoustic model to estimate the intensity and spatial distribution of the microbarom source. The model results elucidate origins of infrasound signals from the tropical cyclone waves as well as their interactions with the ambient conditions consisting of swells, wind seas, and storm waves from nearby systems. The positive correlation between the IS59 observations and the theoretical microbarom estimates, and the saturation of recorded signals from high-energy sources support the use of infrasound signals for inference of tropical cyclone waves.

Citation: Stopa, J. E., K. F. Cheung, M. A. Garcés, and N. Badger (2012), Atmospheric infrasound from nonlinear wave interactions during Hurricanes Felicia and Neki of 2009, *J. Geophys. Res.*, *117*, C12017, doi:10.1029/2012JC008257.

1. Introduction

[2] A variety of anthropogenic and natural sources produce infrasound below the audible threshold of 20 Hz around the globe. Microseisms and microbaroms with a dominant frequency of ∼0.2 Hz are of interest to studies of marine storms. Microseisms, which propagate through the earth, have been recorded by seismometers across the continents. *Benioff and Gutenberg* [1939] were among the first relating microseism generation to ocean waves and later *Gilmore and Hubert* [1948] linked seismograms recorded across North America to tropical cyclones observed in the Pacific Ocean. *Longuet-Higgins* [1950] derived the theoretical framework of microseism generation from nonlinear interactions of ocean waves with equal frequency and opposite directions. With this theoretical framework, *Kedar et al.* [2008] computed the spatial distribution of microseisms over the North Atlantic from the spectral wave model WAVEWATCH III (WW3) of *Tolman et al.* [2002] and related the source intensity and locations of extratropical storms to seismometer records. Since standing waves represent an important source of microseisms, *Ardhuin et al.* [2011] extended the work of *Kedar et al.* [2008] by including reflection of ocean waves from landmasses.

[3] The nonlinear wave interaction described by *Longuet-Higgins* [1950] also produces microbaroms, which propagate through the atmosphere to far distances. *Ponomaryov et al.* [1998] traced the microbaroms measured at Irkutsk, Russia, to oceanic sources and inferred their generation by standing waves trailing behind a tropical cyclone. *Willis et al.* [2004] and *Hetzer et al.* [2008] respectively identified strong microbarom signals in the wake of extra-tropical and tropical cyclones from measurements at International Monitoring System (IMS) infrasound arrays IS59, Kailua-Kona, Hawaii, and IS39, Palau. Analysis of the global WW3 data in both studies linked their measurements to interactions between storm and ambient waves. *Stopa et al.* [2011a] conducted a parametric study with a high-resolution WW3 model and the acoustic model of *Waxler and Gilbert* [2006] to investigate the microbarom source mechanism within a tropical cyclone. Their idealized examples free from ambient waves demonstrate strong dependence of the microbarom distribution on the forward speed as theorized by *Longuet-Higgins* [1950]. The maximum microbarom source was traced to the rear-left quadrant, where previously and locally generated waves with similar frequency bands propagate in opposite directions.

[4] Previous studies have examined microbarom sources either from within an idealized tropical cyclone wavefield or from interactions between storm and ambient waves, but an

[1]Department of Ocean and Resources Engineering, University of Hawaii at Manoa, Honolulu, Hawaii, USA.
[2]Hawaii Institute of Geophysics and Planetology, University of Hawaii at Manoa, Kailua-Kona, Hawaii, USA.

Corresponding author: K. F. Cheung, Department of Ocean and Resources Engineering, University of Hawaii at Manoa, Honolulu, Hawaii, USA. (cheung@hawaii.edu)

Table 1. Compiled Data for Hurricane Felicia of 2009[a]

Time (UTC)	LON (deg)	LAT (deg)	Vmax (m/s)	Pres (mb)	Rmw (km)	Vf (m/s)	Class
08–04 12:00	235.1	12.0	25.7	1000	22.2	7.1	TS
08–04 18:00	233.9	12.2	33.4	987	33.3	6.1	C1
08–05 00:00	233.2	12.6	36.0	985	25.9	4.1	C1
08–05 06:00	232.3	13.2	43.7	975	37.0	5.5	C2
08–05 12:00	231.6	13.7	51.4	955	37.0	4.3	C3
08–05 18:00	230.7	14.2	59.2	948	37.0	5.2	C4
08–06 00:00	229.9	14.7	64.3	935	37.0	4.7	C4
08–06 06:00	229.2	15.1	64.3	935	37.0	4.0	C4
08–06 12:00	228.5	15.7	61.7	940	37.0	4.6	C4
08–06 18:00	227.7	16.2	59.2	948	37.0	4.7	C4
08–07 00:00	226.8	16.7	59.2	948	37.0	5.1	C4
08–07 06:00	226.0	17.2	54.0	956	37.0	4.7	C3
08–07 12:00	224.8	17.7	48.9	967	33.3	6.4	C2
08–07 18:00	223.7	18.1	43.7	973	33.3	5.8	C2
08–08 00:00	222.6	18.6	46.3	970	33.3	6.0	C2
08–08 06:00	221.3	18.9	43.7	973	33.3	6.5	C2
08–08 12:00	219.9	19.2	41.2	975	33.3	7.0	C1
08–08 18:00	218.6	19.6	38.6	981	33.3	6.6	C1
08–09 00:00	217.3	19.9	38.6	982	33.3	6.5	C1
08–09 06:00	216.0	20.2	36.0	984	22.2	6.5	C1
08–09 12:00	214.7	20.5	30.9	994	22.2	6.5	TS

[a]Time (UTC), location (LON, LAT), maximum sustained wind speed (Vmax), surface pressure (Pres), radius of maximum winds (Rmw), forward speed (Vf), and class (TS = tropical storm, C1 = category 1 tropical cyclone, etc).

investigation of their combined effects on recorded infrasound signals is not evident. This paper describes an effort to examine microbarom sources from combined tropical cyclone and ambient wavefields and their correlation with infrasound measurements in the central North Pacific from Hurricanes Felicia and Neki of 2009. We utilize the nested global and Hawaii regional WW3 model of *Stopa et al.* [2011b] to reconstruct the background wind waves and swells as well as the high-resolution tropical cyclone wavefield. The infrasound model of *Waxler and Gilbert* [2006] allows elucidation of both microbarom source mechanisms as well as their interpretation in the recorded infrasound signals at IS59, Kailua-Kona, Hawaii. In this paper, section 2 provides a narrative of these two storm events and an initial examination of the recorded infrasound signals. Section 3 summarizes the suite of wind, wave, and microbarom models used in the analysis. This gives the technical background for interpretation of model results and correlation with measurements. Section 4 describes validation of the computed wavefields with altimetry data, while section 5 compares the computed microbaroms to measurements from IS59 to help identify the source mechanisms. Last, section 6 provides a summary of the findings in light of the predicted and recorded data.

2. Tropical Cyclone and Infrasound Data

[5] Hurricanes Felicia and Neki were intense tropical cyclones in the central North Pacific that tracked near Hawaii in the 2009 storm season. The National Weather Service (NWS) publishes the best track information including the location, central pressure, and maximum sustained wind speeds of the tropical cyclones. This is supplemented by the radius of maximum winds determined by forecasters at the Honolulu office from satellite images, model results, and reconnaissance aircraft measurements during the events. Tables 1 and 2 summarize the compiled storm data for Hurricanes Felicia and Neki in Coordinated Universal Time (UTC).

[6] Hurricane Felicia occurred at the peak of the storm season with multiple events in the central North Pacific. Figure 1 shows the best tracks of Felicia and an adjacent

Table 2. Compiled Data for Hurricane Neki of 2009[a]

Time (UTC)	LON (deg)	LAT (deg)	Vmax (m/s)	Pres (mb)	Rmw (km)	Vf (m/s)	Class
10–20 18:00	196.3	13.9	30.9	1000	18.5	7.2	TS
10–21 00:00	195.2	15.0	33.4	992	13.9	7.9	C1
10–21 06:00	194.3	15.9	38.6	985	37.0	6.4	C1
10–21 12:00	193.6	16.6	46.3	975	44.4	5.0	C2
10–21 18:00	193.4	17.6	51.4	960	44.4	5.2	C3
10–22 00:00	193.3	18.3	54.0	956	46.3	3.6	C3
10–22 06:00	193.3	19.0	54.0	956	46.3	3.6	C3
10–22 12:00	193.4	19.7	51.4	965	46.3	3.6	C3
10–22 18:00	193.6	20.4	46.3	970	46.3	3.7	C2
10–23 00:00	193.8	21.1	43.7	970	46.3	3.7	C2
10–23 06:00	194.1	21.9	41.2	980	41.7	4.4	C1
10–23 12:00	194.4	22.5	30.9	995	41.7	3.4	TS
10–23 18:00	194.6	22.9	28.3	998	41.7	2.3	TS

[a]Time (UTC), location (LON, LAT), maximum sustained wind speed (Vmax), surface pressure (Pres), radius of maximum winds (Rmw), forward speed (Vf), and class (TS = tropical storm, C1 = category 1 tropical cyclone, etc).

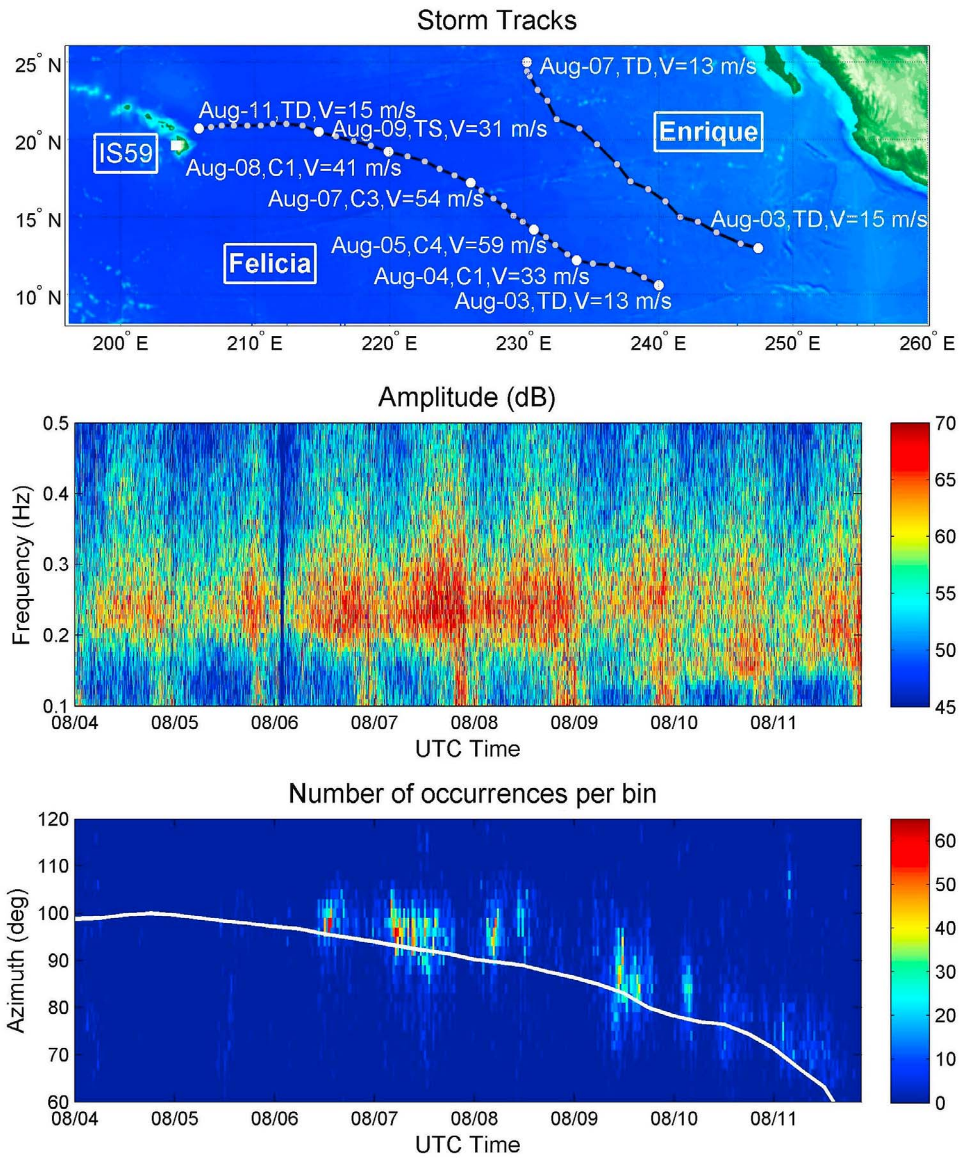

Figure 1. Recorded storm and infrasound data during Hurricane Felicia of 2009. (top) The tracks of Hurricane Felicia and Tropical Storm Enrique and (middle) the spectrogram of the recorded microbarom signals at IS59. (bottom) The azimuth of PMCC3 detections and the storm track (white line) relative to IS59, showing the majority of the energy is generated in the wake of the tropical cyclone.

storm as well as the recorded data at IMS infrasound array IS59. Felicia became a category 1 tropical cyclone with an estimated radius of maximum winds of 25 km and a maximum sustained wind speed of 33 m/s on August 4. As it intensified into category 4 heading toward Hawaii on August 5, reconnaissance aircrafts measured a radius of 37 km and a maximum sustained wind speed of 58 m/s. The storm continued its WNW track until it was downgraded to category 1 on August 8 with a radius of 33 km and a wind speed of 41 m/s. Felicia continued to weaken and reached Hawaii on August 11 as a tropical depression. Tropical Storm Enrique, which formed a day prior to Felicia, moved slowly to the NW on a parallel track from August 4–7. The ambient wind and wave conditions were fairly typical of the late summer. The trade winds were 5–10 m/s from the ENE and relatively weak swells came from the SSW with wave periods of 10–18 s. When Felicia's remnants passed over the island on August 11, the trade winds were severely slackened by the low pressure.

[7] Hurricane Neki approached Hawaii from the south in the late tropical cyclone season of the central North Pacific. Figure 2 shows its best track and the recorded infrasound data at IS59. The storm became a category 1 tropical cyclone on October 21 and intensified into category 3 later that day with the radius of maximum winds increased rapidly to 44 km and the maximum sustained wind speed to 51 m/s. It peaked at category 3 on October 22 with 54 m/s wind speed and a radius of 46 km. Neki was downgraded to a tropical storm on October 23 with a radius of 41 km as it slowly weakened and moved north of Hawaii. The trade wind

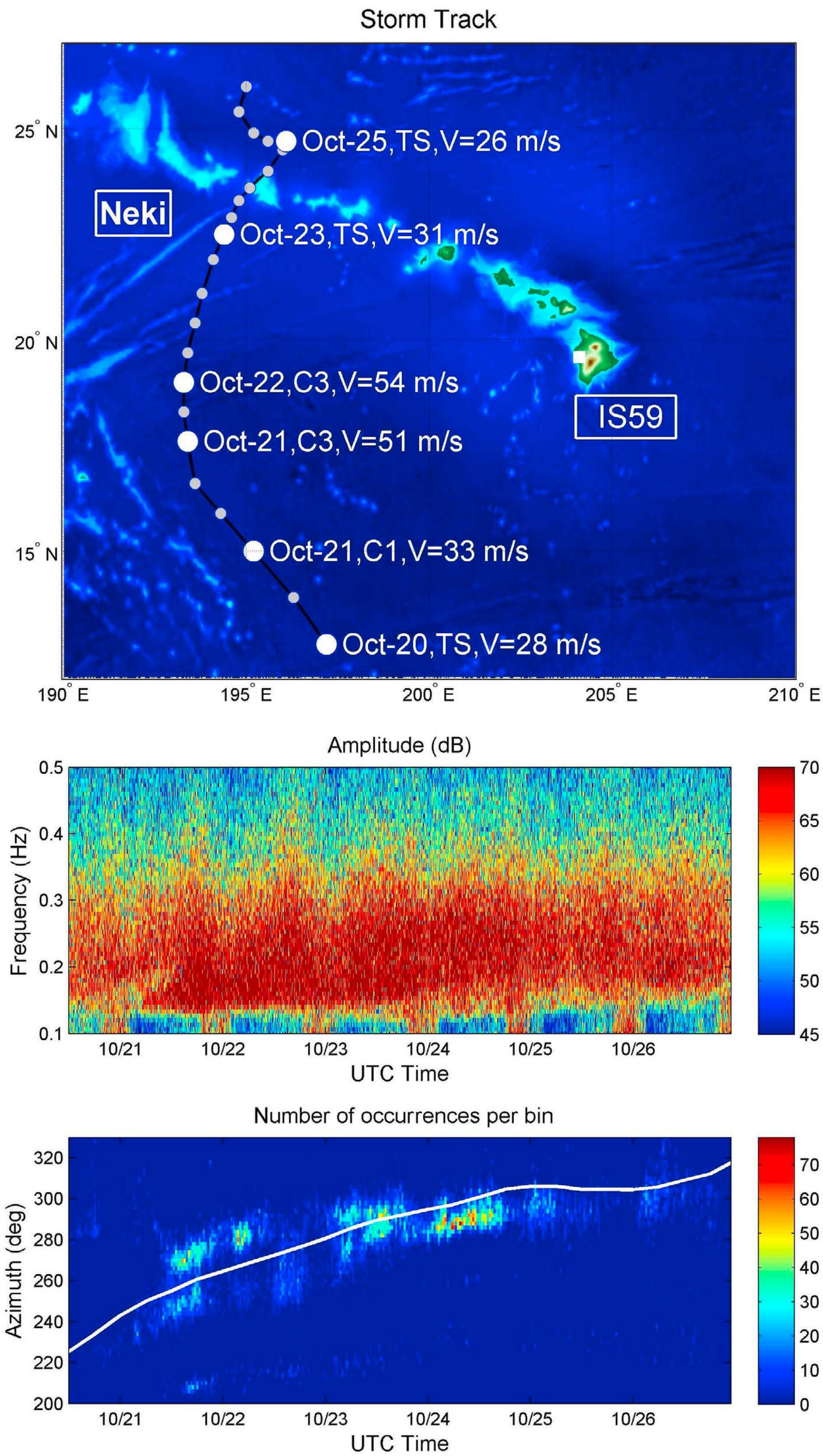

Figure 2. Recorded storm and infrasound data during Hurricane Neki of 2009. (top) The track of Hurricane Neki and (middle) the spectrogram of the recorded microbarom signals at IS59. (bottom) The azimuth of PMCC3 detections and the storm track (white line) relative to IS59, showing the majority of the energy is generated in the wake and in front of the tropical cyclone.

conditions were typical at 5–10 m/s from the ENE during the entire event. This is a transitional month with increased wave activity in the North Pacific [*Arinaga and Cheung*, 2012]. A small NW swell was present with the wave period declining from 14 to 10 s during October 21–24. In addition, small SSW swells were present with wave periods of 10–18 s.

[8] The microbaroms generated by nonlinear interactions of opposing waves would have to propagate through the tropical cyclone to the atmosphere and diffract around mountains to reach IS59 on the west side of Hawaii Island. Propagation of infrasound over telesonic distances depends to a large degree on the wind conditions aloft and to some degree the boundary layer at the station. Some of the more tractable propagation effects related to topography and boundary layers at IS59 are discussed in *Garcés et al.* [2004] and *Willis et al.* [2004]. A separation of the propagation effects through the cyclonic winds and the troposphere, stratosphere, and thermosphere has not been attempted. Additional work is needed to incorporate temperature and wind effects in modeling infrasound propagation through the atmosphere for correction of measurements in the far field. As an initial attempt to investigate the source mechanism, the raw data recorded by IS59 is analyzed for direct correlation with the hindcast microbarom source.

[9] Figures 1 (middle) and 2 (middle) are spectrograms covering the microbarom band of 0.1–0.5 Hz. The modulation of the ambient noise is associated with diurnal wind variations. Figures 1 (bottom) and 2 (bottom) show infrasonic arrivals obtained from post-processing of the array data with the Progressive MultiChannel Correlation, V3 (PMCC3) method [*Cansi and Le Pichon*, 2008]. The PMCC algorithm detects coherent infrasonic energy across the array that allows estimation of the speed, azimuth, and amplitude of the detected acoustic arrivals as a function of time. The arrival azimuths relative to station IS59 are binned into 15 min windows and 2° angular intervals for display. The white line indicates the azimuth of the storm track. For Felicia, the majority of the coherent signals have a greater azimuth indicating the generation of the infrasound behind the storm. For Neki, there are coherent signals on either side of the storm indicating infrasound generated in front and behind the storm. The two tropical cyclones, which had different characteristics and background weather patterns, produced distinct data sets of microbarom signals for the case study.

3. Data and Model System

[10] We utilize a suite of global and regional data sets as well as numerical and parametric models to reconstruct the microbaroms generated by Hurricanes Felicia and Neki of 2009. A blended data set of the global, regional, and tropical cyclone winds is assembled to define the forcing for spectral wave modeling during the two events. Regional nested grids covering the two tropical cyclone tracks are imbedded in the NOAA global WW3 model to compute the wave energy spectrum, which in turn defines the microbarom signal distribution using the infrasound source model of *Waxler and Gilbert* [2006].

3.1. Background and Tropical Cyclone Winds

[11] Accurate representation of the basin-wide wind flows as well as the cyclonic winds of Hurricane Felicia and Neki is the key to modeling the wavefield for microbarom generation. The global wind conditions during the two events are available from the final (FNL) gridded analysis data set of the National Centers for Environmental Prediction. The FNL winds are derived from the Global Forecast System (GFS), which is a spectral model with $0.5° \times 0.5°$ spatial resolution on the earth surface and 64 layers extending to the top of the atmosphere [*Yang et al.*, 2006]. The global data assimilation system incorporates surface winds derived from scatterometers into GFS on a real-time basis [*Chelton and Freilich*, 2005; *Leslie and Buckley*, 2006], and FNL incorporates data from the Global Telecommunications System as well. The resulting wind data is transformed onto a regular $1° \times 1°$ grid at 6-h intervals: 0000, 0600, 1200, and 1800. FNL has proven to give an accurate description of the winds for hindcasting of global wave conditions [*Arinaga and Cheung*, 2012].

[12] The Hawaii archipelago modifies the NE trade wind flow and creates localized weather patterns. The FNL data has provided the initial and boundary conditions to the Weather Research and Forecast (WRF) model to describe the weather along the island chain [*Zhang et al.*, 2005]. The WRF model is based on the non-hydrostatic, three-dimensional Euler equation in the sigma vertical coordinate [*Skamarock*, 2004]. This regional domain covers 194–210°E and 16–26°N to model the upstream wind flow and the modified wind field downstream of Hawaii. The 6-km grid spacing resolves the physical processes important to describe the regional wind field, and the data is output at the standard 10-m elevation every hour. *Stopa et al.* [2012] merged the global FNL and Hawaii WRF data sets to provide forcing for WW3 and validated the resulting wave data with measurements from 12 buoys around Hawaii. The WRF forcing is essential for the wind waves near Hawaii that become important for microbarom generation as Neki tracked across the trade wind flows downstream of Hawaii.

[13] Accurate representation of the tropical cyclone wind, especially near the storm center, is important. Although the background wind field contains effects of the cyclones, the storm tracks and wind structures are not well reproduced in the global model. The vortex of most tropical cyclones is clearly defined and can be represented by a parametric model with concentric circles of isotachs. These types of empirical models describe tropical cyclone wind fields through the storm parameters and thus are referred to as parametric to distinguish from physics-based models. *Phadke et al.* [2003] extended the modified Rankine vortex model with spirally inward wind flows and storm forward speed, and along with *Tolman and Alves* [2005] and *Cheung et al.* [2003, 2007], showed the resulting parametric model produces an accurate description of tropical cyclone wind fields for ocean wave modeling. This parametric model provides a convenient tool to generate the wind conditions from the best track, maximum sustained wind speed, and radius of maximum winds from NWS. In this study, we blend the parametric wind fields of Hurricanes Felicia and Neki into the merged global FNL and Hawaii WRF data set

for hindcasting of the wave conditions. Great care is taken to ensure integrity of the storm inner core and continuity of the cyclonic and background wind fields in the blended data set.

3.2. Waves and Microbaroms

[14] WW3 (version 3.14) is a third-generation spectral model for wave generation and propagation from deep to intermediate water under prescribed wind-forcing [*Tolman et al.*, 2002; *Tolman*, 2008]. The phase-averaged model evolves the wave energy density N (with units of m^2) over frequency f, direction θ, time t, and space. The governing action-balance equation, when written in spherical coordinates of latitude and longitude (ξ, ψ), is given by

$$\frac{\partial N}{\partial t} + \frac{1}{\cos\xi}\frac{\partial}{\partial \xi}\dot{\xi}N\cos\theta + \frac{\partial}{\partial \psi}\dot{\psi}N + \frac{\partial}{\partial k}\dot{k}N + \frac{\partial}{\partial \theta}\dot{\theta}N = \frac{S}{\sigma} \quad (1)$$

where k is wave number, $\sigma = 2\pi f$ is intrinsic angular frequency, the over-dot represents the rate of change, and S denotes the source terms for nonlinear effects such as wind-wave interactions, quadruplet wave-wave interactions, and dissipation through whitecapping, bottom friction, and wave breaking. The directional wave energy spectrum (with units of m^2/Hz) is obtained from $F(f, \theta) = N(k, \theta)/\sigma$ through a Jacobian transform from k to f. The significant wave height is defined as

$$H_s = 4\sqrt{\int_0^\infty \int_0^{2\pi} F(f,\theta)d\theta df} \quad (2)$$

which is a measure of the total energy of the sea state. The spectral peak defines the peak period and peak direction, which together with the significant wave height provide a description of the sea state.

[15] We implement the NOAA global WW3 at 1° × 1.25° resolution in hindcast mode and incorporate in it a two-way nested regional domain covering the entire track of each tropical cyclone at 6-min (~11 km) resolution. The computed wave spectrum is resolved by 25 frequency bins from 1.1 to 0.04167 Hz (periods of 0.9–24 s) and 36 directional bins of 10° each. The global and regional grids are constrained by landmasses and ice concentrations and forced with a blended wind data set from FNL, WRF, and the parametric model. The global model is run for two weeks prior to each event to ensure a developed sea state for the given wind conditions. The wind friction factor is directly related to the amount of energy transferred from the winds to the waves and is accounted for in the source term by a semi-empirical formula from *Tolman and Chalikov* [1996]. The common practice has been to use a wind friction factor that increases with the speed to account for roughening of the ocean surface, but *Powell et al.* [2003] showed that this is correct up to a certain extent beyond which spraying and splashing occur to slow down wave growth. We adopted the cap on the wind friction factor suggested by *Powell et al.* [2003] in WW3 to inhibit waves from increasing to unphysical heights. Reflection is not considered in the wave model as *Ardhuin et al.* [2011] have verified minimal effects offshore of Hawaii.

[16] *Waxler and Gilbert* [2006] developed a two-fluid model to describe radiation of atmospheric microbaroms by nonlinear interactions of ocean waves. The microbarom spectrum is computed from the ocean wave spectrum as

$$D(f_m) = H(f_m)\left(\frac{4\rho_{air}^2 g^2 \pi^4 {f_m}^3}{c_{air}^2}\right)\left(\frac{9g^2}{4\pi^2 c_{air}^2 {f_m}^2} + \frac{c_{air}^2}{c_{water}^2}\right) \quad (3)$$

in which

$$H(f_m) = \int_0^{2\pi} F\left(\frac{f_m}{2},\theta\right)F\left(\frac{f_m}{2},\theta+\pi\right)d\theta \quad (4)$$

where f_m denotes the microbarom frequency, g is the acceleration due to gravity, c_{air} and c_{water} are the speeds of sound in air and water, and ρ_{air} and ρ_{water} are the densities of air and water. The function $H(f)$ was first proposed by *Hasselmann* [1963] as a measure of counter propagating waves of equal frequency in a multidirectional sea state. The peak microbarom source energy can be expressed in decibels as

$$MB = 10\ \log_{10}\left[\max(D(f_m)Q(r,f_m)A)/P_{ref}\right] \quad (5)$$

where A is the source area chosen as the computational cell area in m^2, $Q(r, f_m)$ is a range-dependent propagation factor (with units of m^{-2}), which is treated as unity at the source, and $P_{ref} = (20\ \mu Pa)^2$/Hz is the reference spectral level for acoustic signals in air. The MB is a measure of the infrasound source level and does not have a direct relationship with the significant wave height defined by equation (2).

4. Validation of Wave Modeling

[17] The computed wave spectra involve input uncertainties and model idealizations such as the storm parameters and cyclonic wind flow and require validation with measurements before their implementation in the microbarom calculation. Both Hurricanes Felicia and Neki did not pass close to any of the wave buoys around Hawaii, but their wavefields were recorded by the Jason-1 satellite. The polar orbiting satellite has been flying over the Earth from 66°S to 66°N in 254 passes every 10 days since December 2001. Its dual-frequency (C & Ku microwave bands) altimeter measures the sea surface elevation with errors of 3.9 cm. The significant wave height is an intrinsic property of the sea surface measurement that can be estimated from the slope of the leading edge of the returned signal [*Fedor et al.*, 1979]. Typical errors are within ±0.4 m or 10% of the measured values, whichever is larger. There were a number of passes across the nested regional domain during each event. Two passes nearest to the storm are selected for validation. Interpolated significant wave heights from WW3 are compared to along-track gridded values from Jason-1.

[18] Figure 3 presents the computed wavefields of Hurricane Felicia in the regional domain as well as the comparison with measured significant wave heights along the passes during the strengthening and weakening phases on August 5 and 8. The wavefields show the maximum significant wave height on the right side of the track due to the stronger winds associated with the storm forward motion. The arrows indicate the peak direction in the predominantly multimodal sea

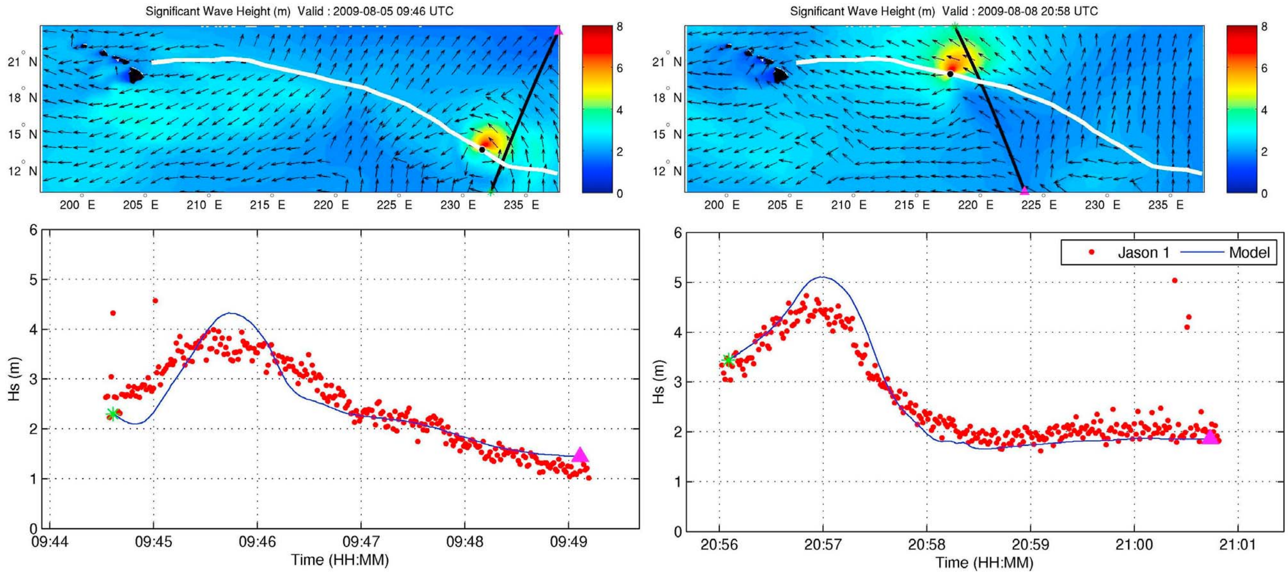

Figure 3. Computed wavefields of Hurricane Felicia and comparisons with altimetry measurements on August 5 and 8. On the bottom panels the red circles represent Jason-1 and the blue line represents the model data. The green circle and pink triangle denote the start and end of the satellite pass across the nested computational domain.

state associated with trade wind waves, swells, and the continuously evolving tropical cyclone waves. Both passes cut through the rear quadrants of the storm with directional spread of the waves over 180° as shown in Hurricane Bonnie of 1998 by *Wright et al.* [2001] and *Walsh et al.* [2002] and in idealized tropical cyclones by *Stopa et al.* [2011a] for microbarom generation. The comparison shows good agreement between the computed and measured data of the tropical cyclone as well as the ambient seas. The model slightly over predicts the peak in both passes by less than 0.5 m, which is at the level of measurement and model errors.

[19] Jason-1 flew over Hurricane Neki at its peak and disintegration phase on October 21 and 26. Figure 4 shows the corresponding wavefields and their comparison with measurements along the satellite tracks. The computed

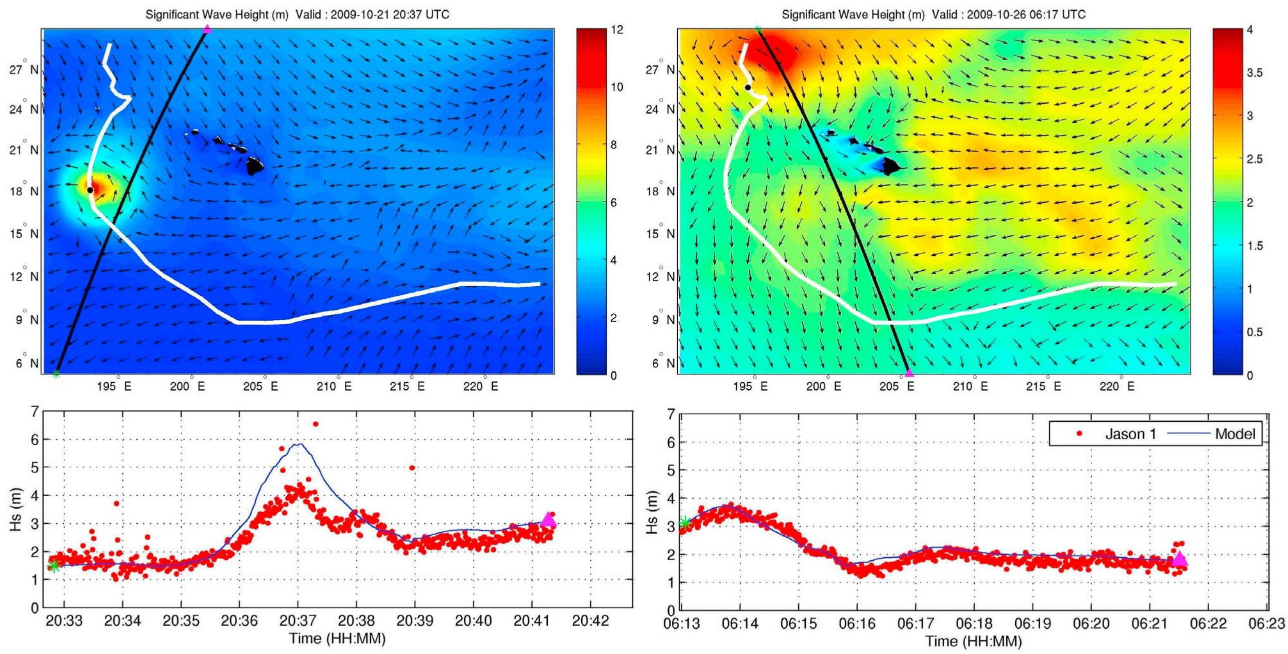

Figure 4. Computed wavefields of Hurricane Neki and comparisons with altimetry measurements on October 21 and 26. On the bottom panels the red circles represent Jason-1 and the blue line represents the model data. The green circle and pink triangle denote the start and end of the satellite pass across the nested computational domain.

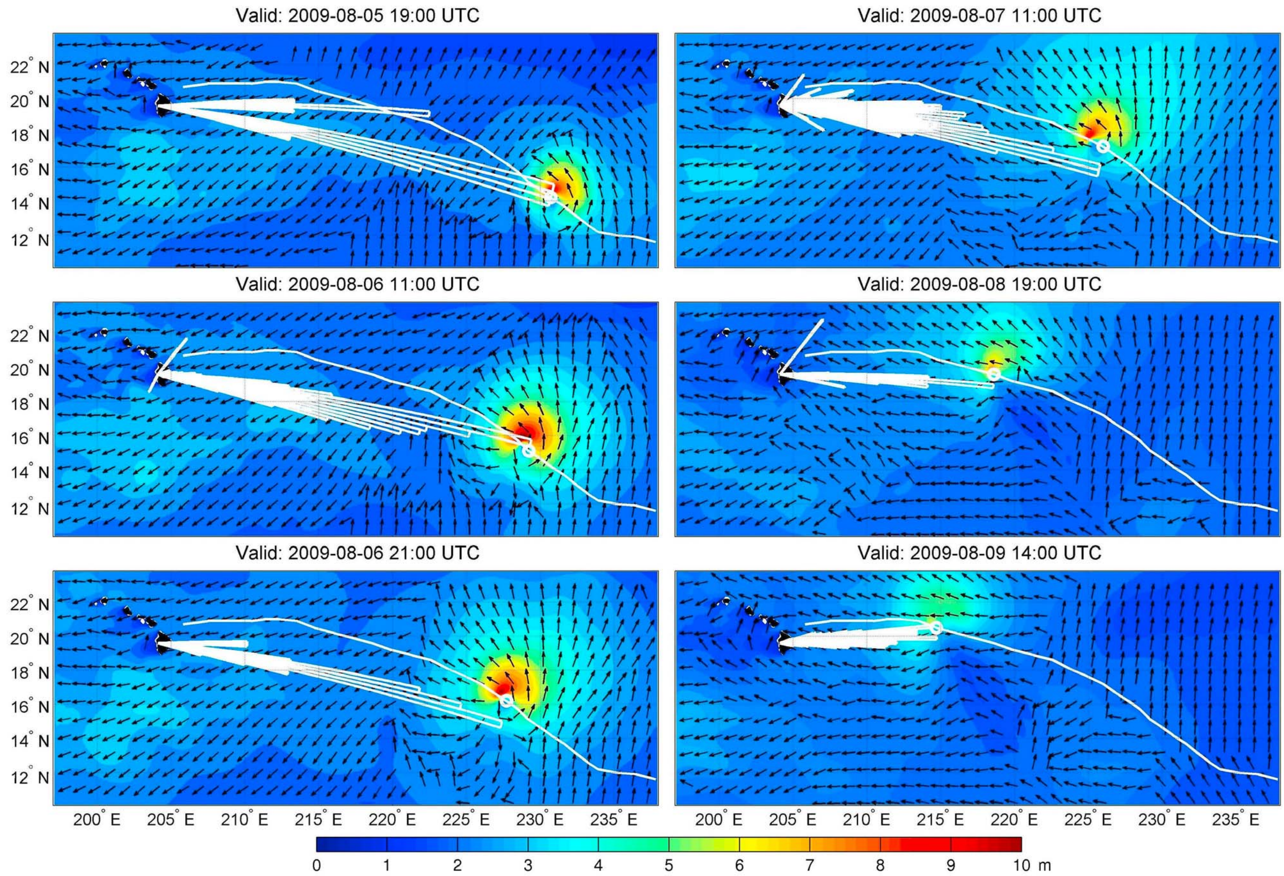

Figure 5. Computed significant wave height and peak wave directions of Hurricane Felicia along with a directional histogram of recorded signals at IS59.

significant wave height reaches 12 m at the peak of the storm, when the satellite passes through the two rear quadrants. The model gives an overall fit to the measurements, but overestimates the wave heights by up to 2 m near the core of the storm. The measured wave height shows considerable scatter and a secondary peak implying the complex structure of the tropical cyclone at this stage. Neki disintegrates after passing north of the Hawaii archipelago into cooler water, but still produces up to 4 m of significant wave height at the core. The merged wind field does a good job in estimating the wave height despite the poorly organized storm at this stage.

[20] The results from a parametric model are directly dependent on the estimation of the storm track, maximum wind speed, and radius of maximum winds. The computed wave height for Hurricane Felicia matches the altimetry measurements well due to a better description of the storm parameters by reconnaissance plane measurements. The over-estimation for Hurricane Neki may be related to the radius of maximum winds, which was estimated by NWS forecasters from model results and satellite images in the absence of reconnaissance plane measurements. The use of FNL and WRF winds resolves the ambient waves from global and regional sources reasonably well in both cases as already demonstrated by *Stopa et al.* [2011b, 2012] through extensive comparisons with buoy and satellite measurements. Although this validation is not extensive and the model appears to have a slightly positive bias, the computed wave data reasonably depicts the tropical cyclone and ambient sea states for estimation of the microbarom sources.

5. Microbarom Source Comparison

[21] Infrasound array IS59 recorded continuous microbarom signals from Hurricanes Felicia and Neki as shown in Figures 1 and 2. The post-processed time series of signal azimuths are binned into 1° increments every hour to produce statistically significant results. The distribution of the azimuth counts are presented in directional histograms from IS59 for comparison with the computed wave and microbarom fields at representative phases of the storms. The timing of the corresponding acoustic signals is accounted for by subtracting the travel time from the storm center to IS59 assuming a sound speed of 343 m/s.

5.1. Hurricane Felicia

[22] Hurricane Felicia approached Hawaii along a WNW track in the open ocean. The resulting wavefield, which is free of reflection or scattering from landmasses, provides a good example to illustrate microbarom generation from tropical cyclones in the central North Pacific. Figure 5 displays the significant wave height distribution and the histogram of azimuth counts as the storm moves toward Hawaii. The length of each bar in the histogram is normalized by the distance from IS59 to the storm center for ease of interpretation. As Felicia expands and intensifies rapidly to category 4

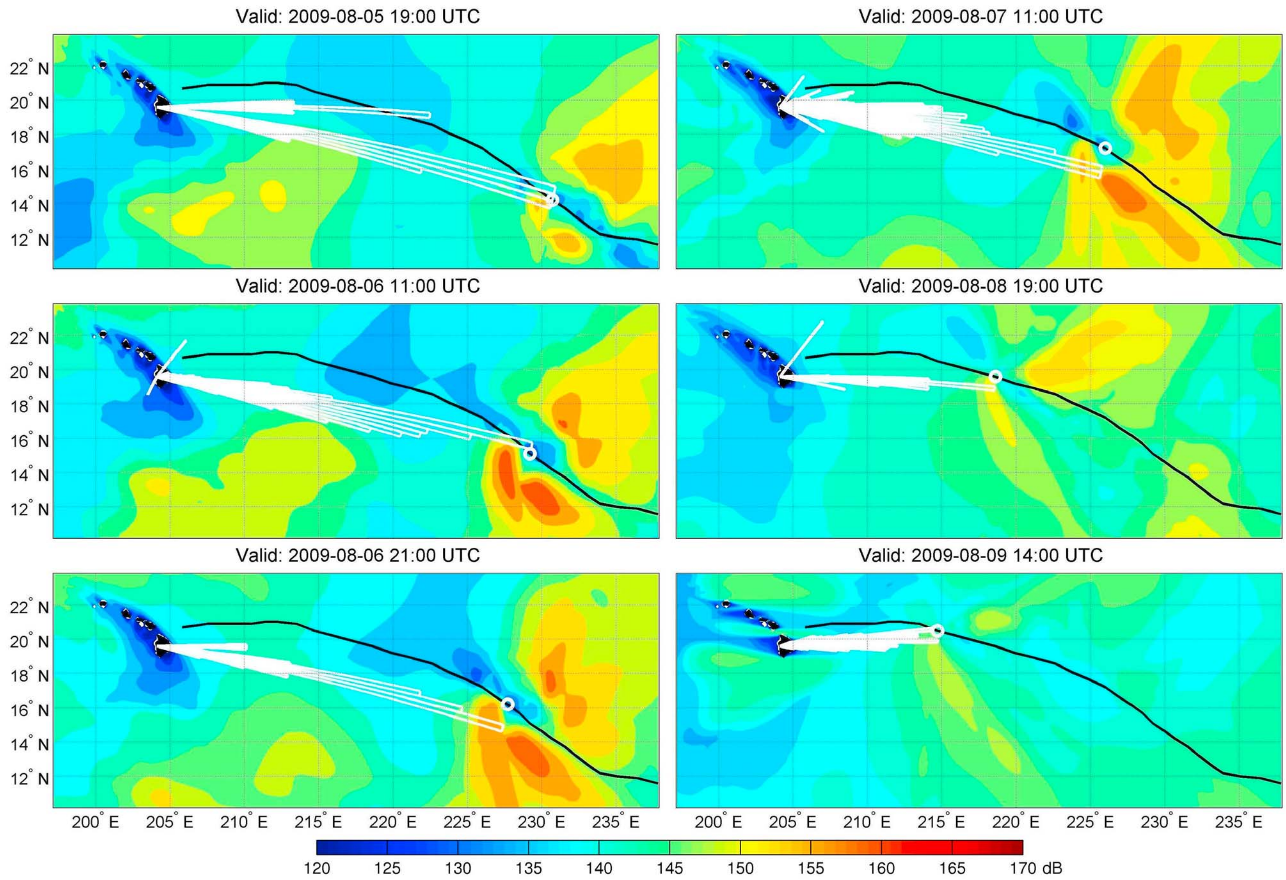

Figure 6. Computed microbarom fields of Hurricane Felicia along with a directional histogram of recorded signals at IS59 focusing on the source regions in the wake of the storm.

on August 5, the wave height on the right quadrants is in excess of 8 m. The peak wave direction reveals trade wind seas from the ENE and a weak south swell in the background of the tropical cyclone waves. The storm reaches its peak with 11 m of wave height on August 6 and begins to weaken later that day, but maintains at least 7 m of wave height through August 7. The declining trend continues as the storm moves north into cooler water with wave heights of 6 and 4 m on August 8 and 9. Throughout the event, the majority of the recorded infrasound signals point to the wake region of the tropical cyclone. This becomes more obvious as the storm moves north and the wake emerges from the vantage point of the infrasound array at Kailua-Kona.

[23] The recorded acoustic signals do not reflect the wave height distribution, but rather the presence of opposing waves at the same frequency. The computed microbarom source energy in Figure 6 provides a better explanation for the directional distribution of the recorded signals at IS59. On August 5, the computed microbaroms display three distinct peaks under the tropical cyclone in contrast to a single peak in the absence of ambient waves [*Stopa et al.*, 2011a]. The majority of the infrasound measurements points to the peak to the left of the storm center, where the tropical cyclone waves propagate into the south swell as shown in Figure 5. As the storm moves forward, the rear quadrant waves interact with the opposing waves generated earlier from the storm center to augment the microbarom production with a peak in the wake. The source region to the right of the track represents interactions of the wavefields produced by Hurricane Felicia and Tropical Storm Enrique, which moved through the region two days prior. The three peaks in the computed microbaroms continue through August 6, when the storm reaches its maximum strength. The azimuth measurements have the majority of the energy over a 15° spread with the maximum occurrences alternating between the peaks to the right and left of the storm.

[24] The weakened storm still maintains three identifiable source regions in the computed microbaroms on August 7. There is significant reduction in the peak immediately to the left of the storm center, where the tropical cyclone waves shift to the SW as shown in Figure 5. The source region associated with the interaction between the wavefields generated by Hurricane Felicia and Tropical Storm Enrique remain strong and extensive despite disintegration of the latter. The bimodal waves in the wake of a tropical cyclone have directions spreading over 280° [*Stopa et al.*, 2011a]. The large directional spread across multiple frequencies facilitates interactions between the storm and ambient waves for microbarom generation. The rear-left quadrant shows an elongated microbarom source with its peak located 180 km

from the storm center. Theoretical calculations from *Stopa et al.* [2011a] place the peak of the microbarom source from self-interactions of tropical cyclone waves at 85 km from the storm center for the given forward speed. The interactions between the storm waves and the south swell are the primary mechanism in producing the elongated microbarom source in the wake. The infrasound measurements have numerous sources all focused between the three peaks within a directional spread ranging 30°. Felicia becomes a tropical storm on August 9. The elongated source in the rear-left quadrant weakens due to lack of a cyclonic wavefield, but the system continues to emit infrasound signals due to interaction of the storm and ambient waves. The measured signals have a reduced directional spread aimed at the storm center.

[25] The recorded infrasound signals covers the three dominant microbarom sources associated with the storm waves generated by Hurricane Felicia and their interactions with waves from Tropical Storm Enrique and the South Pacific. There are, however, only intermittent signals from a source region to the southeast of Hawaii as shown in Figure 6. This source arising from nonlinear interactions of the south swell and the trade wind waves remains visible until August 7, when Felicia interrupts the trade winds to the islands. This region has a relatively weak source compared to those associated with Felicia and is much closer to IS59 with a distance of 760 km in comparison to ~2000 km from Felicia. By assuming the infrasound coming from the storm center leads to timing offset of the signals from this region southeast of Hawaii. In other time steps (not shown in the figure), IS59 recorded energy from these azimuths despite dominance of the microbaroms generated near Felicia. Although infrasound arrays detect signals from multiple sources simultaneously, the strongest source generally saturates the detected signals and stand out in the coherent arrival count. There are exceptions depending on the dynamics of the atmosphere. Waveguide and stratospheric wind instability may contribute to the temporal variability of infrasonic detections from distant sources [*Garcés et al.*, 2004; *Le Pichon et al.*, 2006]. The changing flow conditions, shadowing, and diffraction induced by topographic effects from Hawaii's massive volcanoes may also help explain the intermittent detections of coherent signals from different directions [*Willis et al.*, 2004].

5.2. Hurricane Neki

[26] Hurricane Neki approached Hawaii from the south at the end of the tropical cyclone season, when extratropical storms become active in the North Pacific. This provides a different environmental setting for examination of microbarom generation. Figure 7 plots the significant wave height and infrasound data at representative phases of the storm. There are 4 concurrent events, which can be seen on October 21 0900 UTC, when the category 1 tropical cyclone has a small radius of 18 km and a significant wave height of 6 m. These include (1) storm waves around the eye of Neki, (2) a north swell dominating the upper half of the domain, (3) east wind waves south of Hawaii, and (4) a south swell only discernible near the lower right-hand corner of the domain. The storm rapidly expands and intensifies to category 3 on the same day with a significant wave height of 10.5 m. A typical tropical cyclone wavefield emerges as the speed and fetch increase on the right side of the track. After reaching its peak on October 22, Neki weakens rapidly with the wave height decreased from 11 to 8 m in 8 h and becomes a tropical storm in less than a day. The north and south swells as well as the trade wind waves persist throughout the event from October 21 to 23, but are overshadowed by the storm waves. The recorded microbarom signals initially show two distinct peaks aiming at the forward and rear quadrants that gradually merge into one as the storm moves north.

[27] The computed microbaroms in Figure 8 provide a more vivid explanation to the recorded signals. On October 21 0900, there are two discernible peaks aiming at the wake of the tropical cyclone and a region at the front, where the storm waves propagate against the north swell. The majority of the coherent signals come from the wake with a directional spread of 12°, while the peak at the front has fewer occurrences despite having a larger source area. The rapid intensification of Neki raises the infrasound level by 10 dB in 10 h. The two peaks are more clearly portrayed with nearly equal numbers of coherent observations and their 15° spread covers each of the microbarom sources reasonably well. The general feature is maintained as Neki attains its maximum strength on October 22, 0800. Interactions between the storm waves and the south swell produce an elongated source behind the storm. At 1600, the computed microbaroms still maintain the two distinct source areas, but observations span the entire region over a large directional spread of 35° with the majority of the occurrences from the wake. The azimuth focuses on the peak of an oblong source region approximately 85 km behind the storm center agreeing with the results from *Stopa et al.* [2011a] for a similar storm in the absence of ambient waves. An inspection of the wave spectrum further confirmed that interactions of tropical cyclone waves remain a major source of microbaroms at this stage. Neki rapidly weakens to a tropical storm on October 23. The long-period waves propagating ahead of the storm interact with the north swell to produce a large and intense source area, which generated most of the recorded signals in the remainder of the event.

[28] The recorded infrasound signals from Hurricane Neki share a common pattern with those from Hurricane Felicia under different ambient conditions. Infrasound array IS59 recorded signals from the multiple sources generated by Hurricane Neki along its track. However, a large source area to the north of Hawaii from interactions of the north and south swells produced only intermittent records in the beginning of the event. Likewise, only a few records come from an expanding source area southwest of Hawaii as remnants of the storm waves interact with the northeast wind waves and south swell. The more intense infrasound signals from Neki saturate the microbarom detections at IS59 despite the presence of multiple sources around Hawaii throughout the event. *Hetzer et al.* [2008] also reported dominant sources of infrasound signals at monitoring stations that can be traced to the wake of tropical cyclones in the Pacific. The case studies with Neki and Felicia elucidate the sources of the observed signals and demonstrate the capability of infrasound arrays to identify and track

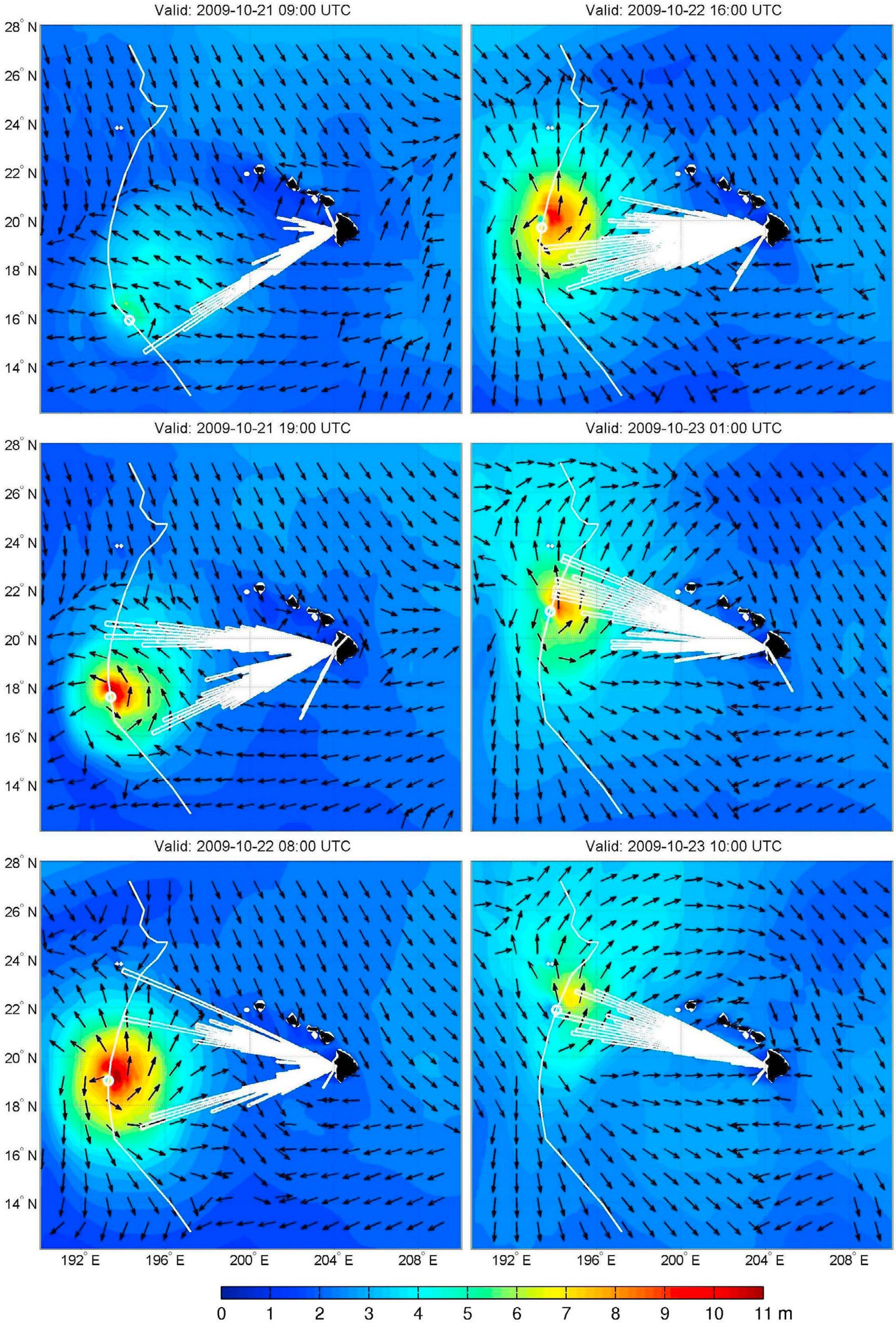

Figure 7. Computed significant wave height and peak wave directions of Hurricane Neki along with a directional histogram of recorded signals at IS59.

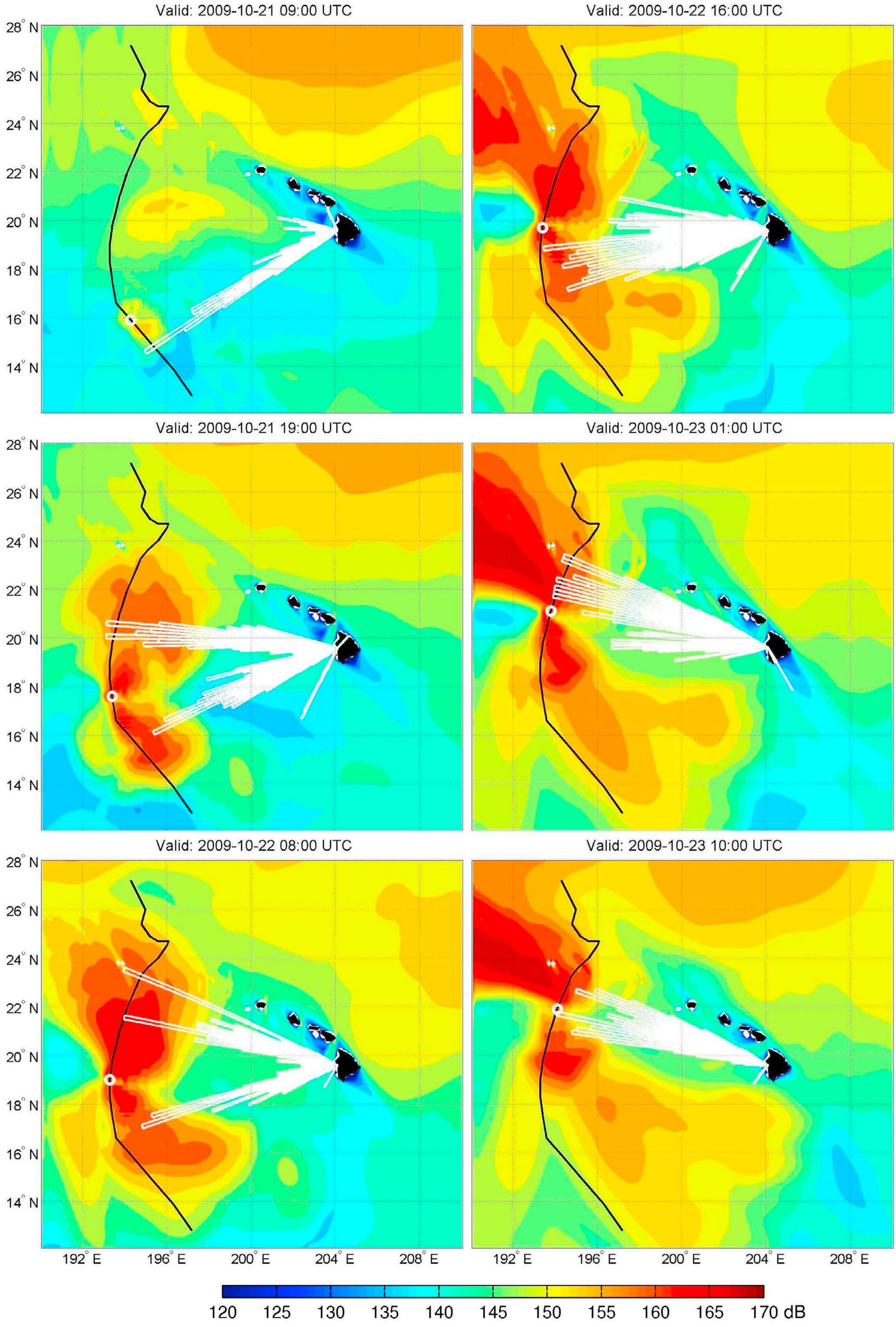

Figure 8. Computed microbarom fields of Hurricane Neki along with a directional histogram of recorded signals at IS59 pointing to the source regions in the wake and front of the storm.

hazardous wave conditions associated with tropical cyclone activities.

6. Conclusions and Recommendations

[29] IMS infrasound array IS59 in Kailua-Kona, Hawaii recorded clear signals from Hurricanes Felicia and Neki of 2009. The two events with distinct storm characteristics and background weather patterns allow investigation of infrasound generation from nonlinear interactions among storm and ambient waves. Blended data sets of global, regional, and cyclonic winds provide a comprehensive description of the forcing for modeling the storm waves as well as the swells and seas commonly seen in the central North Pacific. Regional nested grids imbedded in the NOAA global WW3 model resolve the tropical cyclone wavefields along the tracks. The computed significant wave height is quantitatively compared to altimetry measurements from satellite passes nearest to the tropical cyclones. The modeling approach is able to recreate the observed tropical cyclone and ambient wave conditions for reconstruction of the microbarom sources.

[30] Comparisons of the high-resolution model results with the recorded infrasound signals provide unprecedented details and valuable insights into the generation mechanisms of microbaroms and their detection under tropical cyclone conditions. The forward motion of a tropical cyclone aligns opposing waves generated in the front and rear quadrants to produce a dominant source in the wake as shown by *Stopa et al.* [2011a]. However, the bimodal and broadband waves in the wake interact with ambient waves from multiple directions to produce an elongated source region. Additional sources might develop ahead and on the side of a tropical cyclone when the ambient waves align with the storm waves of equal period in the opposite directions. The infrasound measurements at IS59 corroborate the source mechanisms inferred from the model results and validated the theoretical framework of microbarom generation advanced by *Waxler and Gilbert* [2006].

[31] This study represents an initial step to provide a theoretical explanation for infrasound signals recorded at monitoring stations and to quantify the microbarom sources from tropical cyclones in the open ocean with an abundance of ambient waves. Future research on the propagation mechanism across the atmosphere will improve the correlation between recorded infrasound signals and source energy levels. The microbarom source model should include reflection of ocean waves especially for tropical cyclones adjacent to the coast. With general knowledge on the ambient wave conditions and the microbarom generation mechanism, it is possible to use a network of infrasound arrays to infer tropical cyclone locations and predict hazardous wave conditions. In addition, the saturation of recorded signals from high-energy microbarom sources enables the use of this technology for detection of tropical cyclone waves in sparsely covered regions.

[32] **Acknowledgments.** This paper is funded in part by the National Oceanic and Atmospheric Administration through grant 09-09-022 for the project “Remote Infrasonic Monitoring of Natural Hazards.” We would like to thank the National Weather Service Honolulu Office for the storm data and Yi-Leng Chen for the WRF data around the Hawaiian Islands. We are grateful to David Fee for his participation during the early stages of this research, and to CEA DASE, France, for the use of their PMCC software. We would like to thank the two anonymous reviewers for the comments and suggestions that have improved this paper. SOEST contribution 8722.

References

Ardhuin, F., E. Stutzmann, M. Schimmel, and A. Mangeney (2011), Ocean wave sources of seismic noise, *J. Geophys. Res.*, *116*, C09004, doi:10.1029/2011JC006952.

Arinaga, R. A., and K. F. Cheung (2012), Atlas of global wave energy from 10 years of reanalysis and hindcast data, *Renewable Energy*, *39*, 49–64, doi:10.1016/j.renene.2011.06.039.

Benioff, H., and B. Gutenberg (1939), Waves and currents recorded by electromagnetic barographs, *Bull. Am. Meteorol. Soc.*, *20*, 421–426.

Cansi, Y., and A. Le Pichon (2008), Infrasound event detection using the progressive multi-channel correlation algorithm, in *Handbook on Signal Processing in Acoustics*, edited by D. Havelock, S. Kuwano, and M. Vorländer, pp. 1425–1435, Springer, New York.

Chelton, D. B., and M. H. Freilich (2005), Scatterometer-based assessment of 10-m wind analyses from the operational ECMWF and NCEP numerical weather prediction models, *Mon. Weather Rev.*, *133*(2), 409–429, doi:10.1175/MWR-2861.1.

Cheung, K. F., et al. (2003), Modeling of storm-induced coastal flooding for emergency management, *Ocean Eng.*, *30*(11), 1353–1386, doi:10.1016/S0029-8018(02)00133-6.

Cheung, K. F., L. Tang, J. P. Donnelly, E. Scileppi, K.-B. Liu, X. Z. Mao, S. H. Houston, and R. J. Murnane (2007), Numerical modeling and field evidence of coastal overwash in southern New England from Hurricane Bob and implications for paleotempestology, *J. Geophys. Res.*, *112*, F03024, doi:10.1029/2006JF000612.

Fedor, L. S., T. W. Godbey, J. F. Gower, R. Guptill, G. S. Hayne, C. L. Rufenach, and E. J. Walsh (1979), Satellite altimeter measurements of sea state–an algorithm comparison, *J. Geophys. Res.*, *84*(B8), 3991–4001, doi:10.1029/JB084iB08p03991.

Garcés, M. A., M. Willis, C. Hetzer, A. Le Pichon, and D. Drob (2004), On using ocean swells for continuous infrasonic measurements of winds and temperature in the lower, middle, and upper atmosphere, *Geophys. Res. Lett.*, *31*, L19304, doi:10.1029/2004GL020696.

Gilmore, M. H., and W. E. Hubert (1948), Microseisms and Pacific typhoons, *Bull. Seismol. Soc. Am.*, *38*(3), 195–228.

Hasselmann, K. (1963), A statistical analysis of the generation of microseisms, *Rev. Geophys.*, *1*, 177–210, doi:10.1029/RG001i002p00177.

Hetzer, C. H., R. Waxler, K. E. Gilbert, C. L. Talmadge, and H. E. Bass (2008), Infrasound from hurricanes: Dependence on the ambient ocean surface wave field, *Geophys. Res. Lett.*, *35*, L14609, doi:10.1029/2008GL034614.

Kedar, S., M. Longet-Higgins, F. Webb, N. Graham, R. Clayton, and C. Jones (2008), The origin of deep ocean microseisms in the North Atlantic Ocean, *Proc. R. Soc. A*, *464*(2091), 777–793, doi:10.1098/rspa.2007.0277.

Le Pichon, A., L. Ceranna, M. A. Garces, D. Drob, and C. Millet (2006), On using infrasound from interacting ocean swells for global continuous measurements of winds and temperature in the stratosphere, *J. Geophys. Res.*, *111*, D11106, doi:10.1029/2005JD006690.

Leslie, L. M., and B. W. Buckley (2006), Comments on “Scatterometer-based assessment of 10-m wind analyses from the operational ECMWF and NCEP numerical weather prediction models,” *Mon. Weather Rev.*, *134*(2), 737–742, doi:10.1175/MWR3111.1.

Longuet-Higgins, M. S. (1950), A theory on the origin of microseisms, *Philos. Trans. R. Soc. London A*, *243*(857), 1–35, doi:10.1098/rsta.1950.0012.

Phadke, A. C., C. D. Martino, K. F. Cheung, and S. H. Houston (2003), Modeling of tropical cyclone winds and waves for emergency management, *Ocean Eng.*, *30*(4), 553–578, doi:10.1016/S0029-8018(02)00033-1.

Ponomaryov, E. A., A. G. Sorokin, and V. N. Tabulevich (1998), Microseisms and infrasound: A kind of remote sensing, *Phys. Earth Planet. Inter.*, *108*(4), 339–346, doi:10.1016/S0031-9201(98)00113-7.

Powell, M. D., P. J. Vickery, and T. A. Reinhold (2003), Reduced drag coefficient for high wind speeds in tropical cyclones, *Nature*, *422*, 279–283, doi:10.1038/nature01481.

Skamarock, W. C. (2004), Evaluating mesoscale NWP models using kinetic energy spectra, *Mon. Weather Rev.*, *132*(12), 3019–3032, doi:10.1175/MWR2830.1.

Stopa, J. E., K. F. Cheung, M. A. Garcés, and D. Fee (2011a), Source of microbaroms from tropical cyclone waves. *Geophys. Res. Lett.*, *38*, L05602, doi:10.1029/2010GL046390.

Stopa, J. E., K. F. Cheung, and Y.-L. Chen (2011b), Assessment of wave energy resources in Hawaii, *Renewable Energy*, *36*(2), 554–567, doi:10.1016/j.renene.2010.07.014.

Stopa, J. E., J.-F. Filipot, N. Li, K. F. Cheung, and Y.-L. Chen (2012), Wave energy resources along the Hawaiian Island chain, *Renewable Energy*, in press.

Tolman, H. L. (2008), A mosaic approach to winds wave modeling, *Ocean Modell.*, *25*(1), 35–47, doi:10.1016/j.ocemod.2008.06.005.

Tolman, H. L., and J. H. G. M. Alves (2005), Numerical modeling of waves generated by tropical cyclones using moving grids, *Ocean Modell.*, *9*(4), 305–323, doi:10.1016/j.ocemod.2004.09.003.

Tolman, H. L., and D. V. Chalikov (1996), Source terms in a third-generation wind-wave model, *J. Phys. Oceanogr.*, *26*(11), 2497–2518, doi:10.1175/1520-0485(1996)026<2497:STIATG>2.0.CO;2.

Tolman, H. L., B. Balasubramaniyan, L. D. Burroughs, D. V. Chalikov, Y. Y. Chao, H. S. Chen, and V. M. Gerald (2002), Development and implementation of wind-generated ocean surface wave models and NCEP, *Weather Forecast.*, *17*(2), 311–333, doi:10.1175/1520-0434(2002)017<0311:DAIOWG>2.0.CO;2.

Walsh, E. J., C. W. Wright, D. Vandemark, W. B. Krabill, A. W. Garcia, S. H. Houston, S. T. Murillo, M. D. Powell, P. G. Black, and F. D. Marks (2002), Hurricane directional wave spectrum spatial variation at landfall, *J. Phys. Oceanogr.*, *32*(6), 1667–1684, doi:10.1175/1520-0485(2002)032<1667:HDWSSV>2.0.CO;2.

Waxler, R., and K. E. Gilbert (2006), The radiation of atmospheric microbaroms by ocean waves, *J. Acoust. Soc. Am.*, *119*(5), 2651–2664, doi:10.1121/1.2191607.

Willis, M., M. Garces, C. Hetzer, and S. Businger (2004), Infrasonic observations of open ocean swells in the Pacific: Deciphering the song of the sea, *Geophys. Res. Lett.*, *31*, L19303, doi:10.1029/2004GL020684.

Wright, C. W., E. J. Walsh, D. Vandemark, W. B. Krabill, A. W. Garcia, S. H. Houston, M. D. Powell, P. G. Black, and F. D. Marks (2001), Hurricane directional wave spectrum spatial variation in the open ocean, *J. Phys. Oceanogr.*, *31*(8), 2472–2488, doi:10.1175/1520-0485(2001)031<2472:HDWSSV>2.0.CO;2.

Yang, F., H. L. Pan, S. K. Krueger, S. Moorthi, and S. J. Lord (2006), Evaluation of the NCEP Global Forecast System at the ARM SGP site, *Mon. Weather Rev.*, *134*(12), 3668–3690, doi:10.1175/MWR3264.1.

Zhang, Y., Y.-L. Chen, S. Y. Hong, M. H. Juang, and K. Kodama (2005), Validation of the coupled NCEP mesoscale spectral model and an advanced land surface model over the Hawaiian Islands. Part I: Summer trade wind conditions and a heavy rainfall event, *Weather Forecast.*, *20*(6), 847–872, doi:10.1175/WAF891.1.